Spectral Domain Analysis of Lossy and Nonzero Thickness Dipoles of Finite Length Radiating in Layered Media

Ozzola, Riccardo; Tadolini, Cesare; Neto, Andrea

DOI
10.1109/TAP.2024.3456966

Publication date
2024

Document Version
Final published version

Published in
IEEE Transactions on Antennas and Propagation

Communication

Spectral Domain Analysis of Lossy and Nonzero Thickness Dipoles of Finite Length Radiating in Layered Media

Riccardo Ozzola, Cesare Tadolini, and Andrea Neto

***Abstract*— A spectral domain analysis aimed at studying dipoles radiating in layered media is presented. The model allows for the modeling of the nonzero metal thickness and the reactance associated with a Δ-gap excitation. The solution can be efficiently calculated with a semianalytical procedure, and it is linked to an equivalent circuit representation. The results show an accuracy up to par with commercial solvers regarding the input impedance and the radiated far-field patterns.**

***Index Terms*— Dipole antenna, integral equation, layered media, spectral domain representation.**

I. Introduction

The study of the radiation from electrical dipoles has laid the foundations of computational electromagnetics [1], [2], but still remains a problem of interest [3], [4], [5], [6], [7], [8]. The issue has been investigated both in the spatial [1], [2], [3], [6], [7] and spectral domain [9], [10], [11], [12], often recurring to the *thin* dipole approximation or neglecting the impact of the metal thickness. With the introduction of the transmission line Green's function (TL-GF) [13], [14], [15], such analysis can be performed semianalytically in the spectral domain with a reduced set of unknowns as in [12] and [16]. However, these do not account for the metal thickness, which in the sub-millimeter wave regime can be comparable with the other design parameters. In [17] and [18], for the dual problem of the slots, the impact of the thickness of the metal screen is investigated, and showing an impact even for metallizations in the order of 1/30th of the wavelength. Recently, in [19], the TL-GF, including for the metal thickness, was derived for an infinitely long dipole. This work aims to extend [19] with techniques similar to [12] and [16] to analyze finite dipoles with nonzero metal thickness and to study their input impedance and radiation patterns.

II. Formulation

A. Integral Equation and the Current Spectrum

Let us consider a dipole oriented along the x-axis, embedded in arbitrary stratified media, and constituted by a material of conductivity σ (or equivalently resistivity $\rho = 1/\sigma$), as shown in Fig. 1. It is fed with a voltage V_0 by a Δ-gap generator Δ long located at its center. The dipole has a cross section A, and it is w_y wide and w_z thick and located between $x = -\ell/2$ and $x = \ell/2$. Due to its elongated geometry and the rectangular cross section, only the x-component of the electric field is considered, and this can be written as the product of a longitudinal and a transverse function. The x-component of the incident field e_x^i can be written as follows:

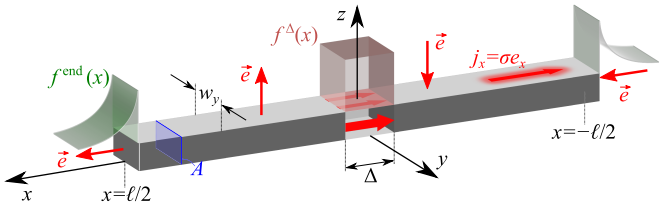

Fig. 1. Sketch of a dipole of length ℓ, width w_y, and thickness w_z, and the representation of the longitudinal distributions on the gap and after the end points.

$$e_x^i(x, y, z) = V_0 f^{\Delta}(x) e_t(y, z) \tag{1}$$

where f^{Δ} and e_t are the excitation's longitudinal and transverse distributions. The x-component of the total electric field e_x can be expressed, for every x and $(y, z) \in A$, by resorting to the local form of Ohm's law as follows:

$$e_x(x, y, z) = \rho i(x) j_t(y, z) \chi_{\text{dip}}(x) + V_{\text{end}} f^{\text{end}}(x) e_t(y, z) \tag{2}$$

where i is the longitudinal current distribution along the dipole, j_t is the transverse current distribution, and χ_{dip} is the characteristic function of the dipole (i.e., $\chi_{\text{dip}} = 1$ for x located in the dipole, and $\chi_{\text{dip}} = 0$ elsewhere). While the first term in (2) models the field in the dipole by means of the local form of Ohm's law, the second one models the field beyond the endpoints. As sketched in Fig. 1, this latter uses the decaying function f^{end}, as in [12] and [16], having amplitude V_{end} at $x = \pm\ell/2$ due to the symmetrical excitation. The x-component of the scattered field e_x^s can be expressed by the following convolution:

$$e_x^s(x, y, z) = g_{xx}^{EJ}\left(x, y, z, z'\right) * \left[i(x)\chi_{\text{dip}}(x) j_t(y, z)\right] \tag{3}$$

where g_{xx}^{EJ} is the xx-component of Green's function providing the electric field from the electric sources located at z' and $*$ denotes the convolutional operator in x and y. Finally, by enforcing $e_x = e_x^i + e_x^s$, one can set the following integral equation for every x:

$$\begin{aligned} &V_0 f^{\Delta}(x) e_t(y, z) - V_{\text{end}} f^{\text{end}}(x) e_t(y, z) \\ &\quad = \left(\rho\,\delta(x, y, z) - g_{xx}^{EJ}\left(x, y, z, z'\right)\right) * \left[i(x)\chi_{\text{dip}}(x) j_t(y, z)\right] \end{aligned} \tag{4}$$

where δ is the Dirac delta. The inner product on the cross section can be defined as follows:

$$\langle f, g\rangle_A = \int\int_A (f)(y, z)\, g^*(y, z)\, dydz \tag{5}$$

which is applied to (4) and $\tilde{j}_t(y, z)$ to obtain the following expression:

$$\begin{aligned} &V_0 f^{\Delta}(x) \left\langle e_t, \tilde{j}_t \right\rangle_A - V_{\text{end}} f^{\text{end}}(x) \left\langle e_t, \tilde{j}_t \right\rangle_A \\ &\qquad = \left\langle \left(\rho\,\delta - g_{xx}^{EJ}\right) * \left[i(x)\chi_{\text{dip}}(x) j_t(y, z)\right], \tilde{j}_t \right\rangle_A \end{aligned} \tag{6}$$

Received 15 April 2024; revised 16 August 2024; accepted 21 August 2024. Date of publication 16 September 2024; date of current version 30 October 2024. *(Corresponding author: Riccardo Ozzola.)*

The authors are with the Department of Microelectronics, Electrical Engineering, Mathematics and Computer Science Faculty, Delft University of Technology, 2628 CD Delft, The Netherlands (e-mail: R.Ozzola-1@tudelft.nl).

Color versions of one or more figures in this article are available at https://doi.org/10.1109/TAP.2024.3456966.

Digital Object Identifier 10.1109/TAP.2024.3456966

where e_t can be assumed to be normalized such that $\langle e_t, \tilde{j}_t \rangle_A = 1$. The right-hand side of (6) can be written as follows:

$$\int\int_A \left(\rho\,\delta(x,y,z) - g_{xx}^{EJ}(x,y,z,z')\right) * \left[i(x)\chi_{\text{dip}}(x) j_t(y,z)\right] \times \tilde{j}_t^*(y,z)dydz. \tag{7}$$

By explicating the convolutional integrals of (7), (8), as shown at the bottom of the next page, is obtained, where in the square brackets the single integral from $-\infty$ to $+\infty$ is performed over dx', and the integrals on the cross section A are performed over dy' and dz'. By interchanging the integration order of dx' and $dydz$, and by calculating the integrals for the Dirac delta, (9), as shown at the bottom of the next page, is found. The terms in curly brackets in (9) allow us to define the transverse Green's function of the dipole $d(x)$ reported in (10) at the bottom of the next page, With the introduction of the transverse Green's function, (6) is written as follows:

$$V_0 f^{\Delta}(x) - V_{\text{end}} f^{\text{end}}(x) = \int_{-\infty}^{+\infty} d\left(x - x'\right) i\left(x'\right) \chi_{\text{dip}}\left(x'\right) dx'. \tag{11}$$

By calculating the Fourier transform of (11) with respect to x, one can write the following expression in the k_x-plane

$$V_0 F^{\Delta}(k_x) - V_{\text{end}} F^{\text{end}}(k_x) = D(k_x) X_{\text{dip}}(k_x) * I(k_x) \tag{12}$$

where F^{Δ}, I, X_{dip}, F^{end}, and D are the Fourier transforms of f^{Δ}, i, χ_{dip}, f^{end}, and d, respectively. The spectrum of the current can be finally written as follows:

$$X_{\text{dip}}(k_x) * I(k_x) = \frac{V_0 F^{\Delta}(k_x) - V_{\text{end}} F^{\text{end}}(k_x)}{D(k_x)}. \tag{13}$$

B. Field Representation

The modeling of the incident field and of the transverse current distribution are congruent with those of [19, eqs. (2), (3), (15), (16), and (27)], allowing to calculate the transverse Green's function with the procedures of [19, eq. (14)]. These use the spectral domain Green's function, which allows the efficient handling of dipoles in layered media.

For the sake of simplicity, field distribution f^{Δ} outside the dipole is assumed to have the following exponential behavior:

$$f^{\text{end}}(x) = \frac{1}{2c}\left(e^{-\frac{x-\ell/2}{c}} u\left(x-\ell/2\right) + e^{\frac{x+\ell/2}{c}} u\left(-x-\ell/2\right)\right) \tag{14}$$

with u being the unitary step function and c being the decay rate, whose value has been determined empirically from CST simulations. For dipoles in free space or located between free space and a low permittivity dielectric, $c = \lambda_0/40$ (where λ_0 is the free-space wavelength at each operating frequency) provides accurate results regardless of the specific geometry. In the case of an high permittivity dielectric, f^{end} requires a faster decay rate than $\lambda_0/40$, due to the smaller confinement of the field. The use of CST has been limited to find empirically the best value of c. Once the value has been determined, it is used in the spectral domain model, independently of CST. The sensitivity of the results with respect to c, and the geometry is discussed in Section III-A.

By calculating the Fourier transform of (14), one obtains the following spectrum:

$$F^{\text{end}}(k_x) = \frac{1}{2}\left(\frac{e^{-jk_x\ell/2}}{1+jk_xc} + \frac{e^{jk_x\ell/2}}{1-jk_xc}\right) \tag{15}$$

which is used to calculate the current spectrum with (13).

C. Method of Moments Solution

The spectrum (13) has only been formally defined, as the weight V_{end}, given the excitation V_0, has still to be determined to calculate the current spectrum of each specific problem. The current distribution i can be obtained from (13) with the following inverse Fourier transform:

$$\begin{aligned} i(x)\chi_{\text{dip}}(x) &= \frac{1}{2\pi}\int_{-\infty}^{+\infty}\left[X_{\text{dip}}(k_x) * I(k_x)\right] e^{-jk_xx} dk_x \\ &= \frac{1}{2\pi}\int_{-\infty}^{+\infty}\frac{V_0F^{\Delta}(k_x) - V_{\text{end}}F^{\text{end}}(k_x)}{D(k_x)} e^{-jk_xx} dk_x. \end{aligned} \tag{16}$$

By calculating the inner product between (16) and a test function $t(x)$, the following expression is derived:

$$\begin{aligned} &\int_{-\infty}^{+\infty}\frac{1}{2\pi}\int_{-\infty}^{+\infty}\left[X_{\text{dip}}(k_x) * I(k_x)\right] e^{-jk_xx} dk_x t^*(x)dx \\ &= \int_{-\infty}^{+\infty}\frac{1}{2\pi}\int_{-\infty}^{+\infty}\frac{V_0F^{\Delta}(k_x) - V_{\text{end}}F^{\text{end}}(k_x)}{D(k_x)} e^{-jk_xx} dk_x t^*(x)dx. \end{aligned} \tag{17}$$

By interchanging the integration order in (17), the Fourier transform of t^* can be calculated as follows:

$$\begin{aligned} &\frac{1}{2\pi}\int_{-\infty}^{+\infty}\left[X_{\text{dip}}(k_x) * I(k_x)\right] T(-k_x)\, dk_x \\ &= V_0\left[\frac{1}{2\pi}\int_{-\infty}^{+\infty}\frac{F^{\Delta}(k_x)T(-k_x)}{D(k_x)} dk_x\right] \\ &\quad - V_{\text{end}}\left[\frac{1}{2\pi}\int_{-\infty}^{+\infty}\frac{F^{\text{end}}(k_x)T(-k_x)}{D(k_x)} dk_x\right] \end{aligned} \tag{18}$$

where T is the Fourier transform of t. By considering t either f^{Δ} or f^{end}, the following two-unknown linear system can be obtained:

$$\begin{cases} V_0 Y_{\Delta,\Delta} - V_{\text{end}} Y_{\Delta,\text{end}} = I_0 \\ V_0 Y_{\Delta,\text{end}} - V_{\text{end}} Y_{\text{end,end}} = I_{\text{end}} \end{cases} \tag{19}$$

where I_0 and I_{end} are the average currents on the gap and beyond the dipole terminations, respectively. The admittances are defined as follows:

$$Y_{m,n} = \frac{1}{2\pi}\int_{-\infty}^{+\infty}\frac{F^m(k_x)F^n(-k_x)}{D(k_x)} dk_x \tag{20}$$

with m and n being either "Δ" or "end."

After having imposed an open-circuit condition outside the dipole, i.e., $I_{\text{end}} = 0$, I_0, and V_{end} can be calculated analytically as follows:

$$V_{\text{end}} = V_0\frac{Y_{\Delta\text{end}}}{Y_{\text{end,end}}} \tag{21}$$

$$I_0 = V_0\left(Y_{\Delta\Delta} - \frac{Y_{\Delta,\text{end}}^2}{Y_{\text{end,end}}}\right). \tag{22}$$

The expression of V_{end} can be used to calculate the current spectrum (13), and I_0 can be used to calculate the input impedance from its definition as follows:

$$Z_{\text{in}} = \frac{V_0}{I_0} = \frac{Y_{\text{end,end}}}{Y_{\Delta\Delta}Y_{\text{end,end}} - Y_{\Delta,\text{end}}^2}. \tag{23}$$

III. Validation and Results

A. Input Impedance

The input impedance is calculated using (23), and an example is shown in Fig. 2(a) and (b), where a good agreement with CST is obtained. However, when the capacitance of the gap becomes

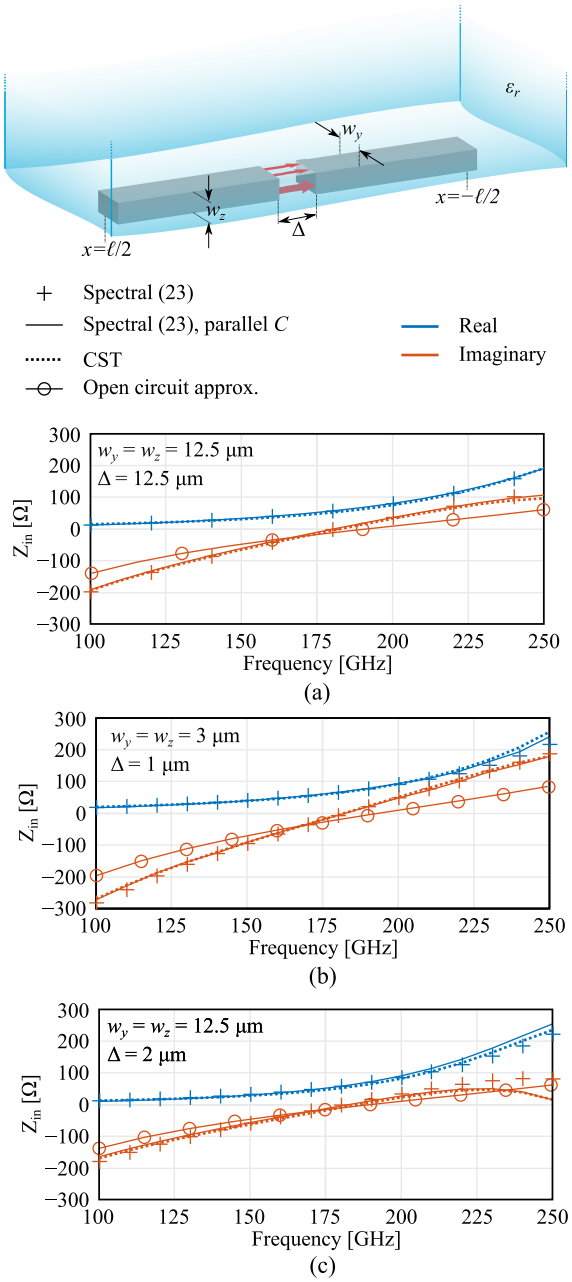

Fig. 2. Input impedance of a dipole having length $\ell = 500$ μm, constituted by a metal having conductivity $\sigma = 10^7$ S/m and printed between free space and a semi-infinite dielectric with relative permittivity $\varepsilon_r = 4$ calculated for (a) $w_y = w_z = \Delta = 12.5$ μm, (b) $w_y = w_z = 3$ μm and $\Delta = 1$ μm, and (c) $w_y = w_z = 12.5$ μm and $\Delta = 2$ μm. The decay rate $c = \lambda_0/40$ has been used.

significant, i.e., the cross section is much larger than the feeding gap, the method becomes inaccurate at high frequencies. In fact, the capacitance of the gap is underestimated in $Y_{\Delta,\Delta}$ as the transverse

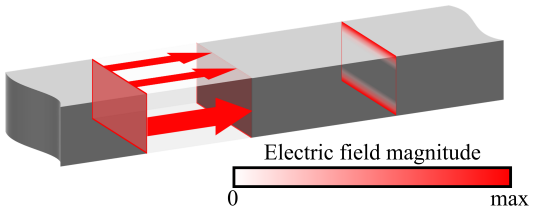

Fig. 3. Sketch of the magnitude of the electric field distribution along the dipole and in the feeding gap.

current distribution $j_t(y, z)$, instead of being uniform, is significant only on the top and bottom part of the two faces of the feeding gap, as shown in Fig. 3. Therefore, an additional parallel capacitance is used to compensate for this effect. This can be approximated with $C = \varepsilon_0 \varepsilon_{\text{eff}} w_y w_z / \Delta$. This compensation is significant in Fig. 2(c), where it improves the comparison with CST.

The low frequency reactance depends on the endpoints located at $x = \pm\ell/2$, and it is associated with the electric field going from one arm of the dipole to the other. This behavior is known to be asymptotic to the open circuit approximation $-jZ_0 \cot(k_{xp}\ell/2)$, where Z_0 and k_{xp} are the characteristic impedance and the propagation constant, respectively, of the line [19]. As it can be seen from Fig. 2, for either the complete solution and the open circuit approximation, the slope of the imaginary part depends on the size of the cross section, as the characteristic impedance Z_0 increases for decreasing values of the cross section [19].

In Fig. 4, the relative error of the input impedance has been calculated with respect to CST, for different geometries and for different values of the decay rate c. The decay rate is shown to be poorly sensitive with respect to the geometry of the dipole, as shown in Fig. 4(a) and (b), while its optimal value decreases with respect to the use of denser dielectrics, as shown in Fig. 4(c) and (d).

Thanks to [19], the proposed spectral domain technique allows for time-efficient dipole simulations accounting for lossy and nonzero thickness metal. Due to the layered media formulation and the semianalytical Green's function, the number of unknowns of (19) does not scale with the ratio between the largest and the smallest dimension of the problem. In Table I, the solution times for the cases of Fig. 2 are reported. The spectral domain approach exhibits improvements in the solution time of at least a factor ten with respect to CST. In addition, the layered media Green's function [20] can also include frequency selective surfaces [21], [22], [23] or artificially engineered materials [24] without increasing the number of unknowns.

B. Current Distribution

The spectrum (16) corrected with the parallel capacitor becomes as follows:

$$X_{\text{dip}}(k_x) * I(k_x) = \frac{V_0 F^{\Delta}(k_x) - V_{\text{end}} F^{\text{end}}(k_x)}{D(k_x)} + j\frac{\omega C V_0 F^{\Delta}(k_x)}{\Delta} \tag{24}$$

where $j\omega C V_0/\Delta$ models the current flowing in the capacitor given the excitation V_0. The function F^{Δ} models the confinement of the

$$\int\int_A \left[\int_{-\infty}^{+\infty}\int\int_A \left(\rho\,\delta\left(x-x', y-y', z-z'\right) - g_{xx}^{EJ}\left(x-x', y-y', z, z'\right)\right) i\left(x'\right)\chi_{\text{dip}}\left(x'\right) j_t\left(y', z'\right) dx'dy'dz'\right] \tilde{j}_t^*(y,z)dydz \tag{8}$$

$$\int_{-\infty}^{+\infty}\left\{\rho\,\delta\left(x-x'\right)\left\langle j_t, \tilde{j}_t\right\rangle_A - \int\int_A\left[\int\int_A g_{xx}^{EJ}\left(x-x', y-y', z, z'\right) j_t\left(y', z'\right) dy'dz'\right]\tilde{j}_t(y,z)dydz\right\} i\left(x'\right)\chi_{\text{dip}}\left(x'\right)dx' \tag{9}$$

$$d\left(x\right) = \rho\delta\left(x\right)\left\langle j_t, \tilde{j}_t\right\rangle_A - \int\int_A\left[\int\int_A g_{xx}^{EJ}\left(x, y-y', z, z'\right) j_t\left(y', z'\right) dy'dz'\right]\tilde{j}_t(y,z)dydz \tag{10}$$

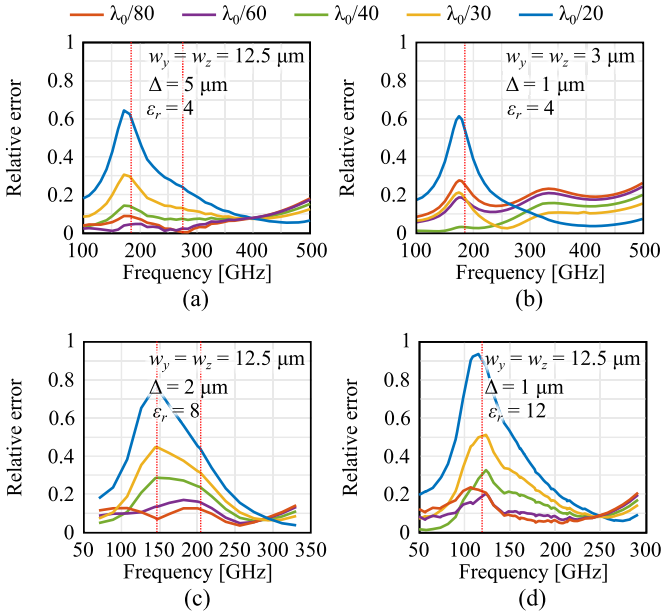

Fig. 4. Relative error of the input impedance calculated with respect to CST for different values of the decay rate c for a dipole $\ell = 500\ \mu$m long, having a feeding gap Δ long, w_y wide, and w_z thick, and printed between free space and dielectric half space with permittivity ε_r. (a) $w_y = w_z = 12.5\ \mu$m, $\Delta = 5\ \mu$m, and $\varepsilon_r = 4$. (b) $w_y = w_z = 3\ \mu$m, $\Delta = 1\ \mu$m, and $\varepsilon_r = 4$. (c) $w_y = w_z = 12.5\ \mu$m, $\Delta = 2\ \mu$m, and $\varepsilon_r = 8$. (d) $w_y = w_z = 12.5\ \mu$m, $\Delta = 1\ \mu$m, and $\varepsilon_r = 12$. The red dashed lines highlight the frequencies for which the imaginary part of the input impedance is null.

TABLE I

SOLUTION TIME FOR THE INPUT IMPEDANCE OF FIG. 2 CALCULATED OVER 16 FREQUENCY POINTS. @INTEL[1] XEON[1] W-2265 CPU @3.5 GHz, 12 CORES, RAM 256 GB

	Case (a)	Case (b)	Case (c)
Spectral	42 s	31 s	51 s
CST (FD solver)[2]	449 s	2023 s	450 s

[2] Finite dielectric of size 1 mm × 0.66 mm × 0.33 mm and *open* boundary on five faces.

displacement currents within the source region, assuming them to be uniformly distributed. An example of the spectrum is given in Fig. 5(a), where the spectra (13) and (24) are compared with 180 GHz for dipoles $\ell = 500\ \mu$m, having cross section $w_y = w_z = 12.5\ \mu$m, printed between free-space and a dielectric half space with relative permittivity $\varepsilon_r = 4$, and excited with $V_0 = 1$ V. The effect of the capacitance C of (24) is to place a high-frequency component, depending on Δ, while leaving untouched the spectrum around k_0. The space current distribution is calculated by performing the inverse Fourier transform of (24), and an example related to the previous study case is shown in Fig. 5(b). While the real part is unaffected by different sizes of the feeding gap, the imaginary part peaks in correspondence with the source region when reducing Δ.

The knowledge of the current spectrum allows for the evaluation of the antenna patterns at $\vec{r} = (r_{\text{obs}}, \theta_{\text{obs}}, \phi_{\text{obs}})$ with the following asymptotic evaluation:

$$\vec{e}^{\,\text{far}}(\vec{r}) \approx jk z_{\text{obs}} \tilde{I}(k_{x\text{obs}}) J_{t,y}(k_{y\text{obs}}) \times \int_0^{w_z} j_{t,z}(z') \bar{\bar{G}}^{\text{EJ}}(k_{x\text{obs}}, k_{y\text{obs}}, z_{\text{obs}}, z') \cdot \hat{x}\, dz' \frac{e^{-jkr_{\text{obs}}}}{2\pi r_{\text{obs}}} \tag{25}$$

[1] Registered trademark.

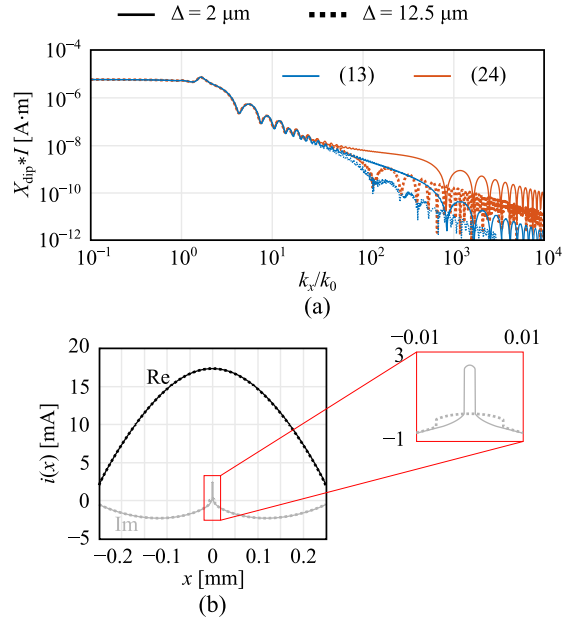

Fig. 5. (a) Spectrum of and (b) spatial distribution of the current at 180 GHz of a dipole having length $\ell = 500\ \mu$m, width and thickness $w_y = w_z = 12.5\ \mu$m, printed between free-space and a semi-infinite dielectric with relative permittivity $\varepsilon_r = 4$, and excited with $V_0 = 1$ V by a Δ-gap generator.

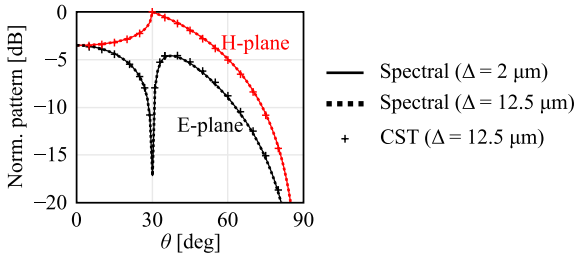

Fig. 6. Far-field patterns at 180 GHz of a dipole having length $\ell = 500\ \mu$m, width and thickness $w_y = w_z = 12.5\ \mu$m, printed between free-space and a semi-infinite dielectric with relative permittivity $\varepsilon_r = 4$, and excited with $V_0 = 1$ V by a Δ-gap generator.

where $k_{x\text{obs}} = k \sin\theta_{\text{obs}} \cos\phi_{\text{obs}}$, $k_{y\text{obs}} = k \sin\theta_{\text{obs}} \sin\phi_{\text{obs}}$, and $k_{z\text{obs}} = k \cos\theta_{\text{obs}}$, $J_{t,y}$ is the spectrum of the current distribution along y, $j_{t,z}$ is the current profile along z', and $\bar{\bar{G}}^{\text{EJ}}$ is the spectral domain Green's function. k_x-current spectrum $\tilde{I}$ is the current spectrum windowed on the dipole, as done in [25, eq. (21)], and calculated as follows:

$$\tilde{I}(k_x) = \mathcal{F}\left\{\mathcal{F}^{-1}\{I(k_x)\}\, \chi_{\text{dip}}(x)\right\} \tag{26}$$

where $\mathcal{F}$ and $\mathcal{F}^{-1}$ denote the Fourier and the inverse Fourier transform operator, respectively. The radiation patterns of Fig. 6 refer to cases of Fig. 2(a) and (c) at 180 GHz. These show the leaky radiation peaks as in [26, Fig. 5] and exhibit an excellent agreement with CST. The two dipoles have the same far-field patterns, despite different sizes of the feeding gap, which impacts the current distribution and the input impedance, different capacitive loading. In fact, Green's function, for observation points sufficiently far away from the sources, filters out the components of the current spectrum above the wavenumber. As shown in Fig. 5(a), the size of the gap and its capacitive loading affect the high part of the spectrum only, and therefore, the far fields are superimposed.

C. Equivalent Circuit

The finite dipole solution allows for the equivalent circuit representation of Fig. 7, which is an extension of [19, Fig. 13]. The dipole

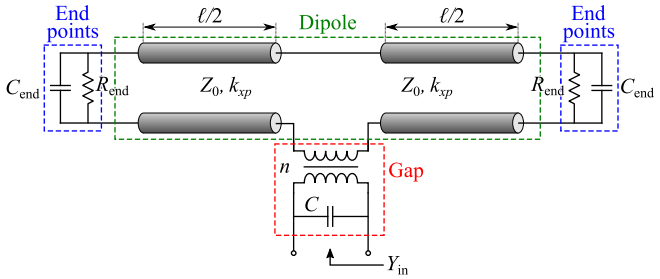

Fig. 7. Transmission line equivalent circuit of a finite dipole, where the contributions of the feeding gap, the dipole, and the end points are highlighted.

can be represented by two transmission line sections of length $\ell/2$, characteristic impedance Z_0, and propagation constant k_{xp}, where Z_0 and k_{xp} have been calculated as in [19]. On either sides, these are loaded with the resistance R_{end} and the capacitance C_{end}, which represent the endpoint radiation and the low frequency capacitance, respectively, and are defined analogously as in [16, eq. (19)]. The gap is modeled by a transformer with turn ratio n and the gap capacitance C. The expression of the former is defined in [19, eq. (37)] and is $n = \sin(k_{xp}\Delta/2)$, while the latter can be modeled as a parallel plate capacitor as in Section III-A.

IV. Conclusion

A spectral domain-based representation of finite dipoles accounting for the nonzero metal thickness was developed. Based on the TLGF [19], the method allows for an efficient semianalytical analysis of the input impedance and the radiation patterns, whose accuracy is up to par with commercial solvers. The developed semianalytical method can provide physical insights into the dipole's current distribution, which is linked to the input impedance and far-field radiation.

References

[1] R. F. Harrington, *Field Computation By Moment Methods*. Hoboken, NJ, USA: Wiley, 1993.

[2] G. Burke and A. Poggio, "Numerical electromagnetics code (NEC)-method of moments; Part I: Program description–theory," Nav. Ocean Syst. Centre, San Diego, CA, USA, Tech. Rep. TD 116, 1981.

[3] L. Knockaert, "Comparing three different formulas for the internal impedance of a circular wire," *Microw. Opt. Technol. Lett.*, vol. 43, no. 1, pp. 1–3, Oct. 2004.

[4] D. R. Wilton and N. J. Champagne, "Evaluation and integration of the thin wire kernel," *IEEE Trans. Antennas Propag.*, vol. 54, no. 4, pp. 1200–1206, Apr. 2006.

[5] N. J. Champagne, D. R. Wilton, and J. D. Rockway, "The analysis of thin wires using higher order elements and basis functions," *IEEE Trans. Antennas Propag.*, vol. 54, no. 12, pp. 3815–3821, Dec. 2006.

[6] D. B. Davidson, "Convergence of the MPIE Galerkin MoM thin wire formulation," *IEEE Trans. Antennas Propag.*, vol. 69, no. 10, pp. 7073–7078, Oct. 2021.

[7] D. B. Davidson and K. F. Warnick, "MoM modeling of thin wires with finite conductivity for radio astronomy applications," in *Proc. IEEE Int. Symp. Antennas Propag. USNC-URSI Radio Sci. Meeting (USNC-URSI)*, Jul. 2023, pp. 769–770.

[8] W. R. Dommisse, J. T. Du Plessis, P. I. Cilliers, M. M. Botha, and T. Rylander, "Macro basis functions for efficient analysis of thick wires in the MoM," *IEEE Trans. Antennas Propag.*, vol. 72, no. 7, pp. 5865–5876, Jul. 2024.

[9] N. Uzunoglu, N. Alexopoulos, and J. Fikioris, "Radiation properties of microstrip dipoles," *IEEE Trans. Antennas Propag.*, vols. AP-27, no. 6, pp. 853–858, Nov. 1979.

[10] I. Rana and N. Alexopoulos, "Current distribution and input impedance of printed dipoles," *IEEE Trans. Antennas Propag.*, vols. AP-29, no. 1, pp. 99–105, Jan. 1981.

[11] N. Alexopoulos and D. Jackson, "Fundamental superstrate (cover) effects on printed circuit antennas," *IEEE Trans. Antennas Propag.*, vols. AP-32, no. 8, pp. 807–816, Aug. 1984.

[12] D. Cavallo, A. Neto, and G. Gerini, "Analytical description and design of printed dipole arrays for wideband wide-scan applications," *IEEE Trans. Antennas Propag.*, vol. 60, no. 12, pp. 6027–6031, Dec. 2012.

[13] C. Di Nallo, F. Mesa, and D. R. Jackson, "Excitation of leaky modes on multilayer stripline structures," *IEEE Trans. Microw. Theory Techn.*, vol. 46, no. 8, pp. 1062–1071, Aug. 1998.

[14] F. Mesa, C. D. Nallo, and D. R. Jackson, "The theory of surface-wave and space-wave leaky-mode excitation on microstrip lines," *IEEE Trans. Microw. Theory Techn.*, vol. 47, no. 2, pp. 207–215, Feb. 1999.

[15] A. Neto and S. Maci, "Green's function for an infinite slot printed between two homogeneous dielectrics. I. Magnetic currents," *IEEE Trans. Antennas Propag.*, vol. 51, no. 7, pp. 1572–1581, Jul. 2003.

[16] R. M. van Schelven, D. Cavallo, and A. Neto, "Equivalent circuit models of finite slot antennas," *IEEE Trans. Antennas Propag.*, vol. 67, no. 7, pp. 4367–4376, Jul. 2019.

[17] J. R. Mosig, "Scattering by arbitrarily-shaped slots in thick conducting screens: An approximate solution," *IEEE Trans. Antennas Propag.*, vol. 52, no. 8, pp. 2109–2117, Aug. 2004.

[18] A. Mazzinghi, A. Freni, and M. Albani, "Influence of the finite slot thickness on RLSA antenna design," *IEEE Trans. Antennas Propag.*, vol. 58, no. 1, pp. 215–218, Jan. 2010.

[19] E. A. Speksnijder, R. Ozzola, and A. Neto, "Spectral domain Green's function of an infinite dipole with non-zero metal thickness and rectangular cross-section," *IEEE Trans. Microw. Theory Techn.*, vol. 72, no. 8, pp. 4530–4541, Aug. 2024.

[20] W. H. Syed, D. Cavallo, H. T. Shivamurthy, and A. Neto, "Wideband, wide-scan planar array of connected slots loaded with artificial dielectric superstrates," *IEEE Trans. Antennas Propag.*, vol. 64, no. 2, pp. 543–553, Feb. 2016.

[21] S. Monni, G. Gerini, A. Neto, and A. G. Tijhuis, "Multimode equivalent networks for the design and analysis of frequency selective surfaces," *IEEE Trans. Antennas Propag.*, vol. 55, no. 10, pp. 2824–2835, Oct. 2007.

[22] F. Costa, A. Monorchio, and G. Manara, "Efficient analysis of frequency-selective surfaces by a simple equivalent-circuit model," *IEEE Antennas Propag. Mag.*, vol. 54, no. 4, pp. 35–48, Aug. 2012.

[23] F. Mesa, M. García-Vigueras, F. Medina, R. Rodríguez-Berral, and J. R. Mosig, "Circuit-model analysis of frequency selective surfaces with scatterers of arbitrary geometry," *IEEE Antennas Wireless Propag. Lett.*, vol. 14, pp. 135–138, 2015.

[24] D. Cavallo and C. Felita, "Analytical formulas for artificial dielectrics with nonaligned layers," *IEEE Trans. Antennas Propag.*, vol. 65, no. 10, pp. 5303–5311, Oct. 2017.

[25] A. J. van Katwijk, A. Neto, G. Toso, and D. Cavallo, "Efficient semi-analytical method for the analysis of large finite connected slot arrays," *IEEE Trans. Antennas Propag.*, vol. 71, no. 1, pp. 402–410, Jan. 2023.

[26] D. B. Rutledge and M. S. Muha, "Imaging antenna arrays," *IEEE Trans. Antennas Propag.*, vols. AP-30, no. 4, pp. 535–540, Jul. 1982.